

NUMERICAL INVESTIGATION ON THE EFFECT OF BLADE LOADING ON UNSTEADY SHEET CAVITATION PATTERNS

Jeremy Nahon¹, Mehrdad Zangeneh
University College London
London, UK

Motohiko Nohmi
EBARA Corporation
Fujisawa, Japan

ABSTRACT

A common manifestation of cavitation is the formation of vapour structures on the suction surfaces of blades or impellers in low pressure conditions. The numerical study carried out here seeks to correlate the changes in the behaviour of sheet cavitation to variations in blade geometry. The analysis is run for a two-dimensional stationary cascade, such that focus is placed on the streamwise profile. The loading distribution serves to characterise the geometry in terms of fluid quantities. It determines the rate and amount of work generated across the channel and is directly connected to blade surface pressure.

In this study, the test sample consists of a set of varying blade profiles. Each are characterised by specific loading configurations: fore-loaded, aft-loaded or bespoke distributions. The aim being to study cavity dynamics, time-accurate predictions of the flow are generated. Computations are run through ANSYS Fluent using the URANS formulation and Shear Stress Transport turbulence model. Cavitating flow is treated as a homogeneous mixture, with evaporation and condensation rates provided by the Zwart-Gerber-Belamri transport equation model. A range of behaviours are observed for the cavitation patterns. Variations are found in inception conditions, shape and sheet stability. For the latter, two dynamic regimes are identified with a transition point that varies according to the loading profile. A pair of trade-off relations are also observed: the first relates the hydrodynamic efficiency and suction performance, the second is concerned with suction performance and cavity stability. The results demonstrate the capacity of the loading distribution to affect cavitation dynamics through changes in geometry.

Keywords: sheet cavitation, blade loading, SST, cascade, unsteady, Zwart-Gerber-Belamri.

INTRODUCTION

To understand the mechanisms driving cavitation shedding and erosion efforts are being invested in both experimental and numerical research approaches. The motivation is to generate the expertise needed to build reliable predictive tools and to develop technologies that respond well under cavitating conditions. On the numerical side of research, a large portion of the work is focused on enhancing the accuracy of time-resolved techniques by comparing the effectiveness of cavitation models [1]–[4] or by examining the response to turbulence formulations [5]–[7].

In parallel, time-resolved numerical solutions are used to provide details on flow physics which cannot be captured by measurement. This type of study has been carried out for several well-known hydrofoil geometries including the NACA0015 [8]–[10], NACA66 [11], [12] or Clark-Y [7], [13] and has been key in identifying core phenomena such as fluctuation regimes or the effect of vorticity for external cavitating flows.

Although these works have produced valuable benchmarks, they are bounded in scope by the limited geometry range and lack similarity with turbomachinery flows where pressure gradients are substantially amplified. In the study presented here, the time-accurate numerical methodology is applied to a two-dimensional cascade to replicate the characteristics of axial flow impellers. Previously, Iga *et al.* analyzed the unsteadiness of cavitating cascades but focused only on the ClarkY [4] or on flat blade profiles [14]. Here, the study takes a step further by investigating a set of varying non-zero thickness blade geometries. The aim of this novel approach is to identify the influence of blade profile on the dynamic behavior of cavitation

¹ Contact author: j.nahon@ucl.ac.uk

and to provide insight for designing cavitation efficient machinery.

Currently, only a few efforts have been made to develop geometry solutions to cavitation issues. These are burdened with either unconventional design additions, e.g. hole punching [15], limited geometry characterization and control [16], or methodologies that substantially disrupt the flow field, such as in [17] where the drooped nose produces a non-smooth surface.

Here, four two-dimensional blade profiles of varying camber are investigated. Rather than defining the profiles in terms of the surface coordinates, each one is associated to its specific loading distribution. In turbomachinery, loading is an essential quantity which correlates to the rate of work transmitted to the fluid as it flows through the channel. Furthermore, for cutting-edge design methodologies focused on turbomachinery elements, the loading definition is a crucial component [18], [19].

Our study proceeds by, firstly, characterizing the geometries in terms of their computed loading. To that end, the four cascade cases are run in non-cavitating conditions in steady state mode. Time-resolved computations are then carried out at descending cavitation numbers for each case. Time accurate quantities of interest are connected to both the hydrodynamic performance and to cavitation. For the former, total pressure difference, tangential velocity difference and cascade efficiency are monitored. In terms of cavitation, it is the variations in cavity size and shape that are observed. Spectral and spread analysis is used to measure the dynamic regime of the phenomena. Discrepancies in flow solutions are compared against the loading distributions to isolate the compelling correlations.

CASCADE CONFIGURATION & GEOMETRIES

Non-modifiable cascade features are the blade axial chord length $c = 0.13519 m$ and the solidity ratio $s = \frac{c}{pitch} = 1.5$. These numbers originate from the circumferential geometry of an axial flow pump impeller designed following arbitrary requirements. At design point, the meridional velocity of the incoming flow is $V_f = 10 m/s$ and the impeller rotation is such that $U = 10.47 m/s$ at the shroud where the profile is extracted. These velocity values are used to define the inflow condition of the stationary cascade, regardless of the loading case.

Four blade geometries are put to test in this study and are designated as cases A, B, C and D. The blade surfaces are functions of the camber line and tangential thickness:

$$\alpha^\pm \equiv y - [f \pm T/2] = n \times pitch \quad (1)$$

where f and T are, respectively, the camber and thickness axial distributions. The cases are ordered according to the position of highest camber curvature: from high upstream curvature for case A to high downstream curvature for case D. The loading profiles and geometries are presented in **Error! Reference source not found.** For all four geometries, the leading edge is at the same position.

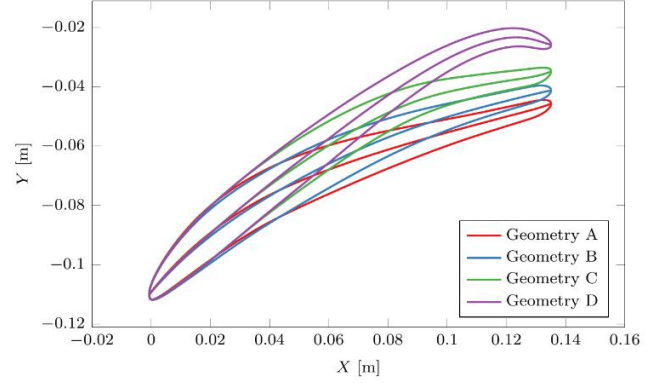


FIGURE 1: 2D BLADE GEOMETRIES; THE CAMBER IS THE CENTERLINE OF THE TANGENTIAL THICKNESS.

NUMERICAL SETUP

Flow solutions are calculated using ANSYS Fluent because the software allows pure 2D configurations and gives the user extensive numerical options. The solver is pressure-based with pressure and velocity calculated simultaneously (coupled rather than segregated algorithm). The Zwart-Gerber-Belamri (ZGB) method [20] is selected for cavitation modelling. It treats cavitating flow as a homogeneous mixture, meaning that density varies according to the advected vapour volume fraction. The ZGB approach is an enhancement of Kubota et al.'s work [21], which uses a simplified form of the Rayleigh-Plesset equation to determine the evaporation and condensation rates:

$$\begin{aligned} \dot{m}_e &= -C_e \frac{3\alpha_{nuc}(1-\alpha_v)\rho_v}{R_B} \left[\frac{2}{3} \frac{p_v - p}{\rho_l} \right]^{1/2} \text{ if } p < p_v \quad (2) \\ \dot{m}_c &= -C_c \frac{3\alpha_v \rho_v}{R_B} \left[\frac{2}{3} \frac{p - p_v}{\rho_l} \right]^{1/2} \text{ if } p > p_v \end{aligned}$$

ZGB parameters are set at default value: $\alpha_{nuc} = 5 \times 10^{-4}$, $R_B = 10^{-6} m$, $C_e = 50$, $C_c = 0.01$. Water is assumed isothermal at $T = 20^\circ C$, such that $p_v = 2339.2 Pa$.

The computational domain consists of a single cascade channel centered around the blade, bounded at the top and bottom by periodic interfaces and by the inlet and outlet openings. The latter are placed at $1 \times c$, for the inlet, and at $4 \times c$, for the outlet, from the leading edge. The mesh is generated using an unstructured quadrilateral topology.

First, steady state computations are run in non cavitating conditions in order to produce the loading profile of geometries A, B, C and D. For steady RANS turbulence closure, the Standard $k - \varepsilon$ model with scalable wall functions is chosen to boost convergence and alleviate computational load. At the blade surfaces, $y^+ < 30$ and the mesh is relatively coarse (20 000 cells).

For time-resolved simulations, the numerical schemes are refined. Turbulence is still modelled through a URANS type methodology rather than DES, LES or DNS, as the latter are too computationally demanding for accurate cavitating flow prediction. Here, the $k - \omega$ SST turbulence closure model is

selected. It is recommended as a reliable technique because of its capacity to properly capture adverse pressure gradients and separated flows which are both features of the cavitation closure region. Because the SST approach is without a wall function, the condition $y^+ < 1$ must be met at all points over the blade walls.

At the inlet, velocity module and direction are imposed. They match the design flow condition i.e. $\|V\| = 14.48 \text{ m/s}$ and $\gamma = 46.321^\circ$. At this speed regime, the wall requirement $y^+ < 1$, demands that the first layer thickness is $y \approx 10^{-6}$. To ensure grid smoothness, the inflation layer contains 75 divisions. The total cell count exceeds 100 000. At the outlet, static pressure is set. It is by lowering the value of the outlet pressure, that cavitation formation is driven.

For time discretization, a second order implicit scheme is applied. Time is advanced by a constant timestep $\Delta t = 5 \times 10^{-5}$, which results in an average Courant number of approximately 0.3. Each physical timestep consists of 50 implicit iterations.

LOADING CHARACTERISATION

In turbomachinery, the amount of work produced by a single stage can be measured as the difference in circumferential velocity ΔrV_θ between inlet and outlet. The loading is the rate of change of rV_θ with respect to the position along a meridional coordinate. For a 2D stationary cascade, rV_θ is substituted for V_y and the velocities are absolute rather than relative. To calculate the loading distribution, it can be shown that [22]

$$p^{PS} - p^{SS} \propto \frac{\partial V_y}{\partial x} \quad (3)$$

The surface pressure and loading profiles are presented in Figure 2 and Figure 3 for all four geometries. All are computed at the same non-cavitating cavitation number $\sigma = 1.369$. To classify the loading profiles, the axial position of the peak is important. Cases A and B fall into the fore-loaded category where the peak is located in the upstream region. Cases C and D are aft-loaded, meaning that the peak is further downstream. There is a strong correlation between the position of highest curvature and highest loading.

In terms of pressure, changes in the distribution on the suction surface are picked up. There is a clear softening of the gradient for aft-loaded cases until the final portion of the blade. Additionally, the minimum pressure value over the surface is lower for the fore-loaded cases.

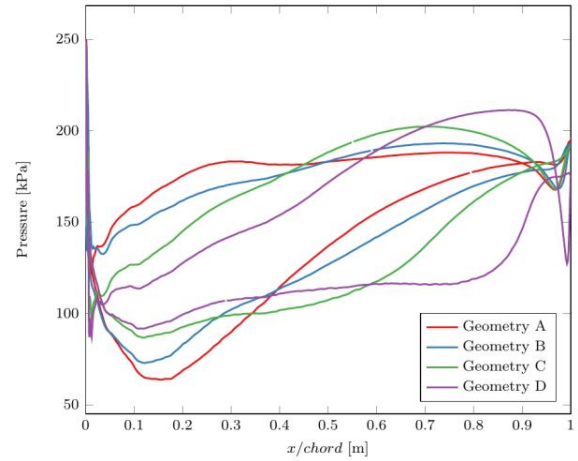


FIGURE 2: STEADY STATE SURFACE PRESSURE IN NON-CAVITATING CONDITIONS ($\sigma = 2.369$).

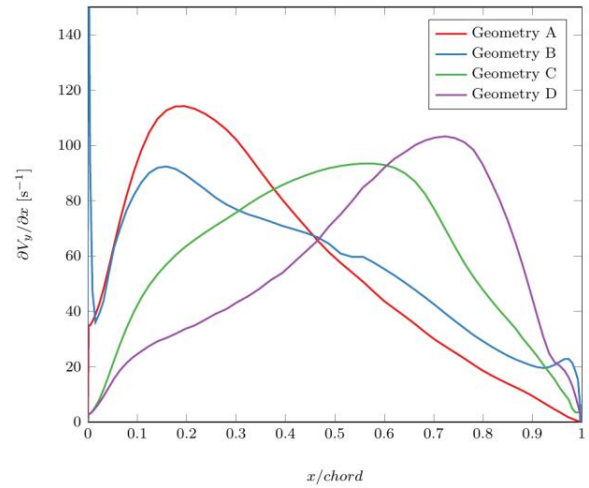


FIGURE 3: BLADE AXIAL/STREAMWISE LOADING.

TIME-RESOLVED SIMULATION RESULTS

All four cases are analyzed for a range of outlet pressures. Each run is carried out for a minimal physical duration of 0.5 s or until the monitored quantities are either stable or fluctuate at a consistent frequency. The tracked quantities are:

- Inlet total pressure,
- Outlet total pressure,
- Outlet mass flow averaged V_y ,
- Total volume of vapor
- Volume averaged turbulent intensity

The role of the listed quantities is to indicate the unsteadiness level or stability of the computation.

1.1 Non-cavitating Conditions ($\sigma \geq 1.8$)

The first set of computations is run for high cavitation numbers such that $p_{min} > p_v = 2339.2 \text{ Pa}$ everywhere over the blade. In Figure 4 and Figure 5 the difference in total pressure between inlet and outlet and the outlet V_y are plotted against time. All geometries produce stable flow fields except for case D. Its

loading profile is strongly aft-loaded, meaning that sharp pressure gradients are found in the downstream part of the blade. In this region, the wall velocity is significantly slowed down so the adverse pressure difference is strong enough to provoke separation (see Figure 6). Spectral analysis of the monitored data for D produces the vortex shedding frequency $f_s = 250 \text{ Hz}$, which corresponds to a Strouhal number $Sr = f_s L / V_\infty = 2.5$. The frequency is greater than what is expected for a cylindrical body at the same Reynolds number $Re \approx 2.5 \times 10^6$ ($0.2 \leq Sr \leq 0.5$).

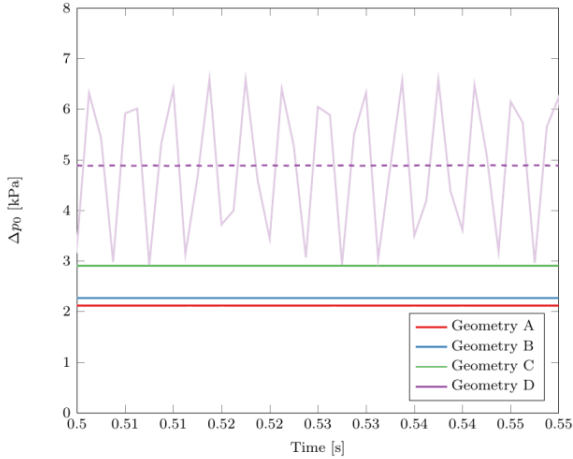


FIGURE 4: TIME HISTORIES FOR THE TOTAL PRESSURE DIFFERENCE BETWEEN INLET AND OUTLET IN NON-CAVITATING CONDITIONS. DASHED LINE FOR CASE D CORRESPONDS TO THE TIME AVERAGED DATA.

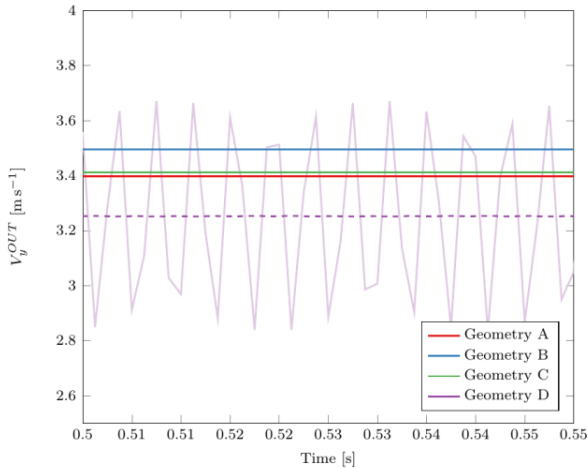


FIGURE 5: TIME HISTORIES FOR THE MASS-FLOW AVERAGED V_y COMPONENT AT OUTLET IN NON-CAVITATING CONDITIONS. DASHED LINE FOR CASE D CORRESPONDS TO THE TIME AVERAGED DATA.

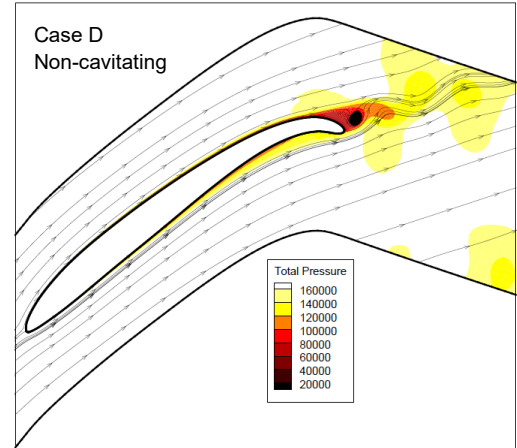


FIGURE 6: STREAMLINES AND TOTAL PRESSURE CONTOURS FOR AFT-LOADED GEOMETRY D IN NON-CAVITATING CONDITIONS. VORTEX SHEDDING CAN BE SEEN AT THE TRAILING EDGE.

Figure 4 also indicates that the total pressure difference Δp_0 is not consistent: fore-loaded cases generate less losses than the aft-loaded ones. Again, this is connected to the position of large pressure gradients over the blade. If close to the leading edge, the boundary layer is thin and changes in pressure are transformed into inertial forces; if closer to the trailing edge, they enlarge the boundary layer and wake or cause separation. This directly affects cascade efficiency, which is obtained by applying

$$\eta = 1 - \frac{\Delta p_0}{\frac{1}{2}\rho(v_y^{in,2} - v_y^{out,2})} \quad (4)$$

Values at $\sigma = 1.369$ (non-cavitating) are given in Table and confirm the superiority of fore-loaded cases in that regard.

TABLE 1: HYDRODYNAMIC PERFORMANCE WITHOUT CAVITATION.

Geometry Case	Δp_0 [Pa]	ΔV_y [m/s]	η
A	2117.4	7.075	0.9567
B	2267.6	6.993	0.9534
C	2905	7.061	0.9406
D	3030	7.211	0.9383

1.1 Cavitating Conditions ($\sigma < 1.8$)

As cavitation starts to appear, fluctuations arise in the monitored data. These fluctuations evolve in size and amplitude with the decrease in outlet pressure. As an example, the total vapour volume histories for runs at different outlet conditions are shown in Figure 7 for cases B and C. The amplitude increases with the mean size of the cavity and the character of the fluctuation tends to become more irregular. To characterise the unsteady data a power spectral density analysis is carried out. The aim is to measure the cyclical behaviour of the cavitating flow by identifying the peak frequency f_C and duration of a single cycle $T_C = f_C^{-1}$. With these numbers, the unsteady

quantities are time averaged and metrics for hydrodynamic performance are produced.

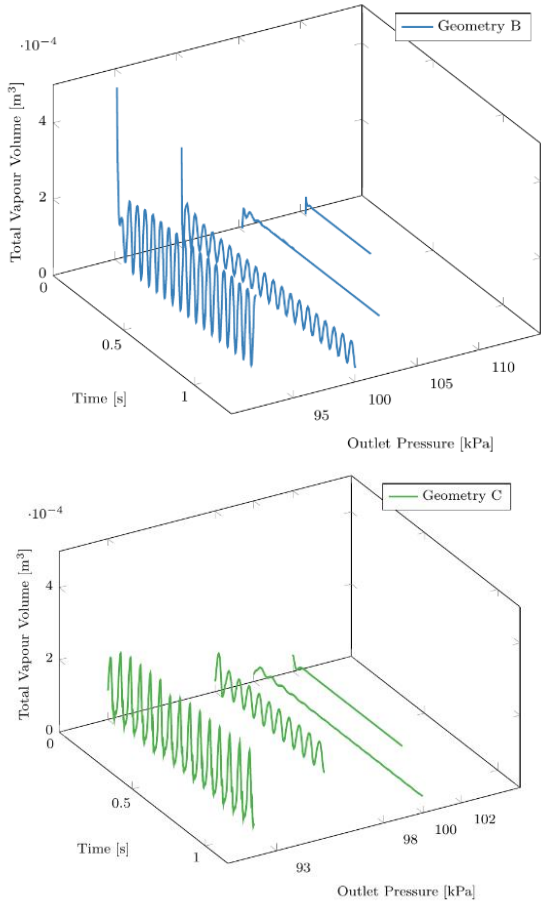


FIGURE 7: EVOLUTION OF VAPOR VOLUME HISTORIES WITH DECREASING OUTLET PRESSURE.

The frequencies resulting from the spectral analysis are presented in Figure 8. An important observation is that the frequency points are grouped into two categories: high frequency ($f_c > 10^2 \text{ Hz}$) and low frequency ($10 \text{ Hz} < f_c < 2 \times 10^2 \text{ Hz}$) unsteadiness. The first is caused by rapid changes in separation zones located either at cavity closure for A, B and C or at the trailing edge for D. The second group of frequencies corresponds to large variations in the size of the sheet cavity. These arise when the re-entrant jet is sufficiently strong to affect the location of the closure region.

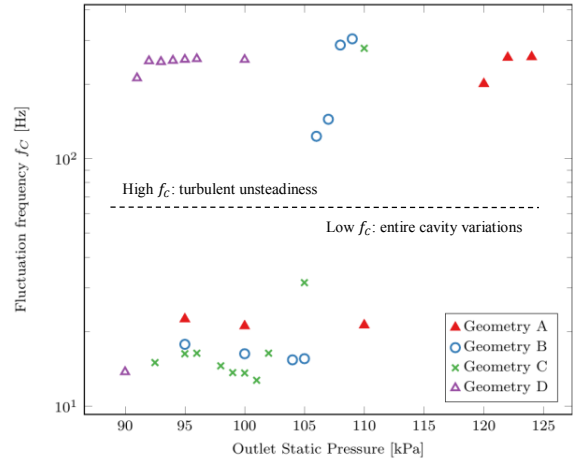
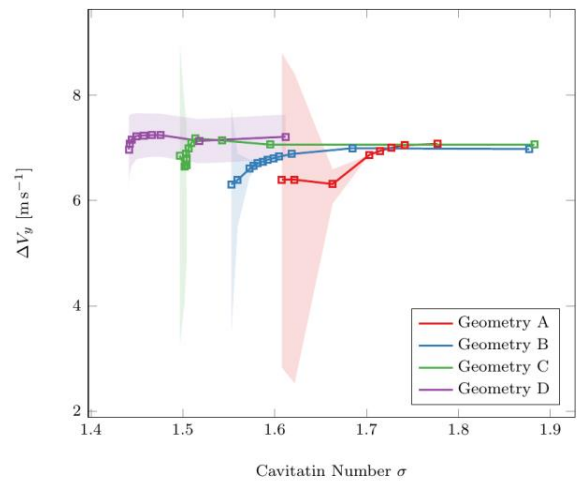


FIGURE 8: PEAK FREQUENCIES OBTAINED FROM THE SPECTRAL ANALYSIS CARRIED OUT ON THE TIME-RESOLVED SOLUTIONS.

The hydrodynamic performance of the cascade is evaluated in terms of the change in tangential velocity ΔV_y , the lift C_L , drag C_D and efficiency η . For stationary cascades, lift and drag are functions of the total pressure difference Δp_0 and velocity vectors at inlet and outlet. The cavitation number for each run is calculated from the time-cycle averaged inlet pressure using the definition $\sigma = (p_\infty - p_v)/0.5\rho V_\infty^2$. Performance metrics are shown in Figure 9 using both mean values and spread of the unsteady data. The σ point at which the ΔV_y or C_L curves drop is a measure of the suction performance. It corresponds to the choking of the channel by the cavity. Because their minimum pressure is higher in non-cavitating conditions, cavitation appears later and aft-loaded geometries C and D achieve better suction results. This means that there exists a trade-off between designing a cascade that delivers high efficiency and one that delivers high suction performance. This relation is important and extrapolates to pump impeller or inducer design.



(5)

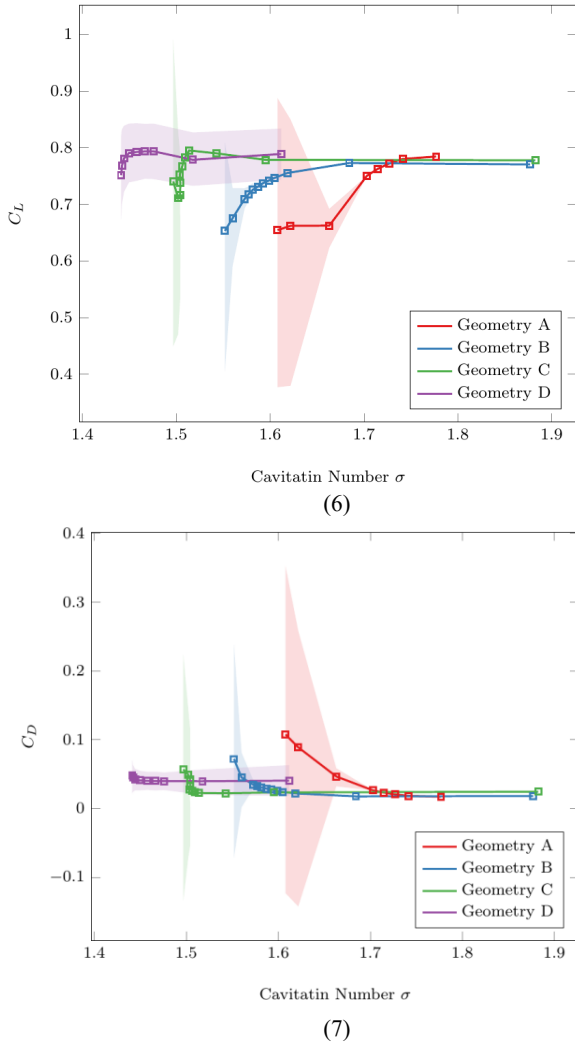


FIGURE 9: ΔV_y (A), C_L (B) AND C_D (C) BREAKDOWN WITH DECREASING CAVITATION NUMBER. THE SOLID LINES ARE TIME-CYCLE AVERAGED, THE SHADED REGIONS ARE MEASURES OF THE SPREAD AND CONTAIN 95% OF THE DATA.

The unsteady simulations provide information on the variability of each datum, which can serve to predict cavitation erosion or vibration [23]. To add to the quantities presented in Figure 9, the growth of the cavity as σ decreases is depicted in Figure 10. An important observation is that the spread is null (stable cavity) before blowing up (unstable cavity). This correlates to the frequency analysis and confirms the two dynamic regimes: (i) stable cavity for σ higher than the transition point, σ_T , and (ii) cyclical growth and collapse for $\sigma < \sigma_T$. This distinction holds true regardless of the loading profile. However, the transition point and amplitude of variations differ. Fore-loaded geometries A and B switch to the second regime for smaller vapour volumes, whereas C and D are able to sustain the stable regime for larger cavity sheets. In terms of spread amplitude, which is equivalent to fluctuation amplitude, the increase is more gradual for A and B. This implies that fore-

loaded cases are more susceptible to suffer from erosion and vibration at high cavitation numbers. The aggressiveness intensifies as the cavity increases in size and in volatility. For aft-loaded geometries, adverse phenomena remain weak at high cavitation numbers ($\sigma > \sigma_T$) but rapidly blow up once in the unstable regime.

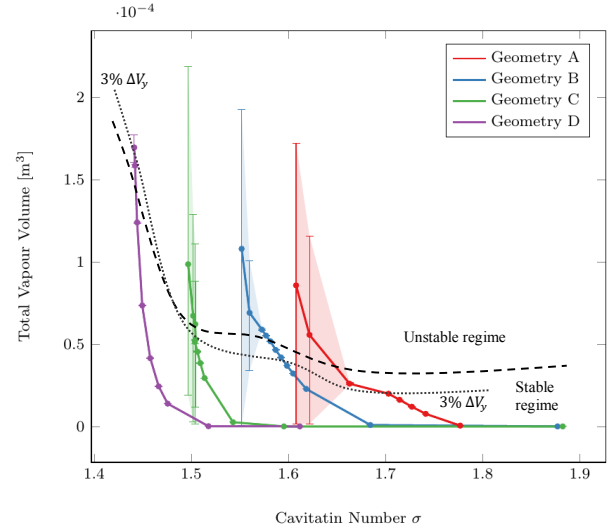


FIGURE 10: GROWTH OF TOTAL VAPOR VOLUME. THE SOLID LINES ARE TIME-CYCLE AVERAGED, THE SHADED REGIONS ARE MEASURES OF THE SPREAD AND CONTAIN 95% OF THE DATA.

In pump operation, the 3%NPSH is an important number which marks the inlet conditions that lead to a 3% drop in head because of cavitation. It is used to standardize comparisons and corresponds to the conventional operational limit for centrifugal impellers [24]. Here, a similar reference point is sought after by considering the 3% drop in ΔV_y and the corresponding cavitation numbers for each case. The inferred $\sigma_{3\%}$ values are listed in **TABLE 2** and a demarcation line is plotted in Figure 10. For fore-loaded cases, the $\sigma_{3\%}$ line is well within the stable regime. As the loading moves downstream, the 3% breakdown point approaches the stable to unstable transition. For case C, the two states coincide, and for D, the cavity is already dynamic when the breakdown occurs.

To complement these observations the shape of the sheet cavities at the same conditions are shown in Figure 11. For the fore-loaded geometries A and B, the vapour sheet is wedge shaped and increases in thickness until closure. The loss in output is due to the superposition of the cavity with the region of highest loading (or curvature). The gradient and amplitude of the pressure recovery at closure are strong (see Figure 12) but because the cavity terminates in a thin boundary layer region where vorticity production is low, the re-entrant jet is too weak to affect the vapor sheet. For the aft-loaded cases, the cavity is forced to extend over an extensive part of the blade in the axial direction before reaching the loading peaks. In that region, vorticity generation is high and, despite a softer pressure

recovery (see Figure 12), the likelihood of seeing strong boundary layer separation and unsteady phenomena is increased.

In Figure 13, the two characteristic cavitation numbers: σ_T for the transition and $\sigma_{3\%}$ for breakdown are plotted together. The advantage of this diagram is that it puts in comparison the corresponding performance criteria: suction performance and cavity stability. Ideally, both $\sigma_{3\%}$ and σ_T will be low, with the added constraint that $\sigma_T < \sigma_{3\%}$ so that stability is ensured even at the lowest operation point, thus reducing the risk or erosion and other adverse effects such as noise or vibration. Considering this, fore-loaded geometry A is far from optimal and aft-loaded case D produces a fluctuating cavity (not to mention the non-cavitating unsteadiness). For geometry C, however, $\sigma_{3\%}$ and σ_T are highly similar suggesting its loading profile delivers an effective compromise.

TABLE 2: CAVITATION NUMBER AT 3% BREAKDOWN FOR CAVITY PATTERN COMPARISON

Geometry Case	$\sigma_{3\%}$	σ_T
A	1.703	<1.663
B	1.587	1.572
C	1.504	1.507
D	1.441	1.455

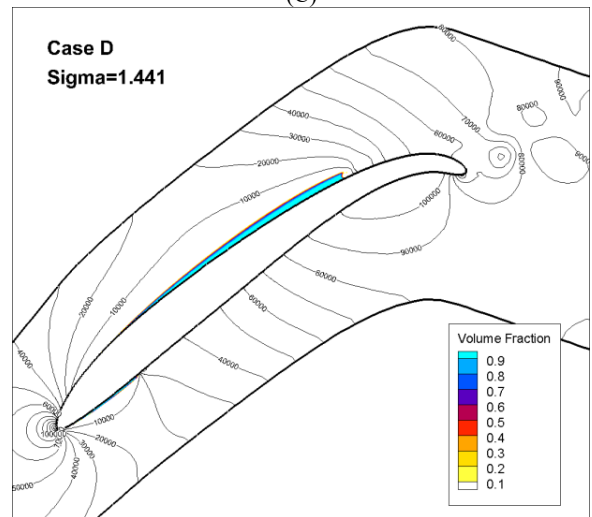
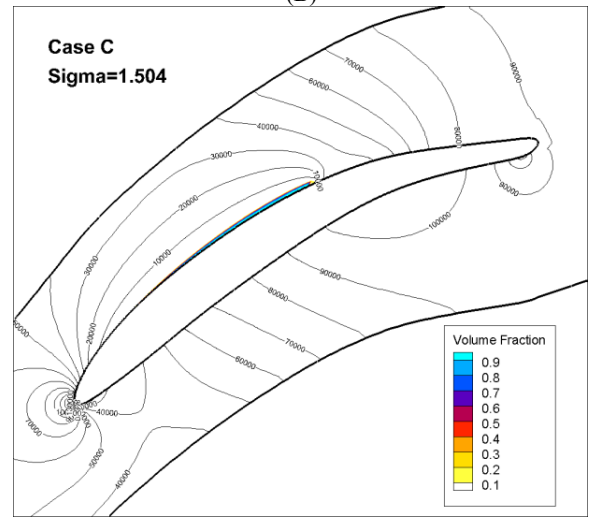
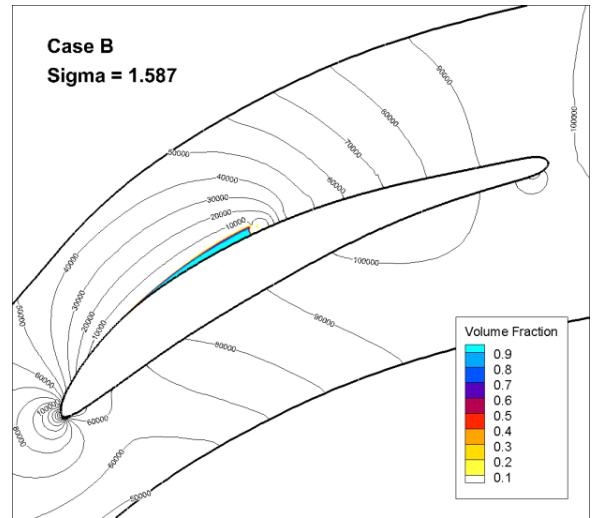
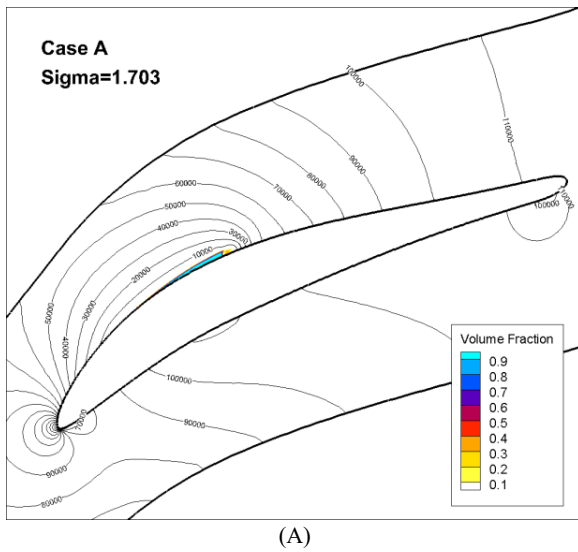


FIGURE 11: INSTANTANEOUS VAPOR VOLUME CONTOURS FOR ALL FOUR CASES AT $\sigma_{3\%}$.

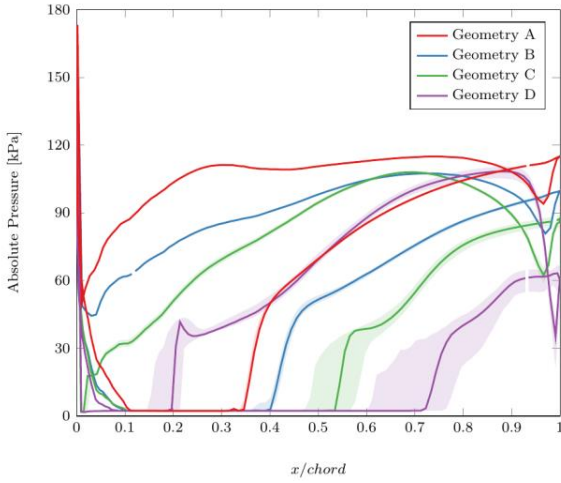


FIGURE 12: UNSTEADY BLADE SURFACE PRESSURE AT $\sigma_{3\%}$. TICK LINES ARE TIME CYCLE AVERAGED, THE COLORED AREAS CORRESPOND TO THE 95% DATA SPREAD.

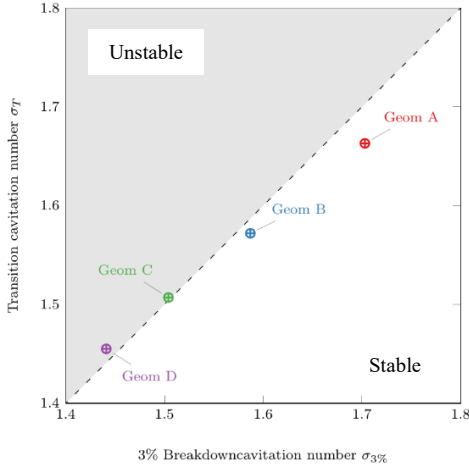


FIGURE 13: COMPARISON OF SUCTION AND CAVITATION STABILITY PERFORMANCE. THE DIAGRAM INDICATES WHETHER THE CAVITY IS STABLE AT THE CASCADE'S LOWEST OPERATING POINT.

CONCLUSION

Time-resolved computations were carried out for four loading profiles at a range of cavitation numbers. The loading distributions went from strongly fore-loaded to strongly aft-loaded. Dynamic data was acquired in both cavitating and non-cavitating conditions and processed to provide performance metrics related to work output (ΔV_y , C_L , C_D , η) or to qualify the unsteadiness of the cavity. The important outcomes of this research are the following observations:

- In non-cavitating conditions, for the same ΔV_y output the aft-loaded geometries deliver higher viscous and turbulent losses than the fore-loaded cases. The efficiency thus decreases with the streamwise position of the loading peak.

- In terms of suction performance, aft-loaded profiles are far more effective. There, therefore, exists a trade-off between high efficiency for non-cavitating flow and suction performance (see Figure 9 and Table 1).
- Sheet cavitation obeys two dynamic regimes: (i) stable, where small-scale unsteadiness is generated by low amplitude turbulent effects, (ii) unstable, when the re-entrant jet perturbs the cavity closure. The transition point between the two regimes varies with blade loading: high σ and small cavity for fore-loaded cases, low σ and large cavity for aft-loaded cases.
- At low operating points ($\sigma_{3\%}$), aft-loaded cases are more prone to unsteadiness because of the downstream position of the cavity closure in a zone where vorticity effects are strong. Here, another trade-off is identified, which sets suction performance against cavity stability and aggressiveness (see Figure 13).

In conclusion, this research has shown that blade loading is a potent variable to correlate blade geometry and cavitation performance. It also demonstrates that the loading profile can serve to affect the behavior of sheet cavities and opens up a new axis of research.

ACKNOWLEDGEMENTS

We would like to thank EBARA Corp., Japan, for their financial and expert support throughout the course of this research. In particular, Dr Goto and Dr Watanabe who have provided excellent and abundant recommendations.

REFERENCES

- [1] M. Morgut, E. Nobile, and I. Biluš, "Comparison of mass transfer models for the numerical prediction of sheet cavitation around a hydrofoil," *Int. J. Multiph. Flow*, vol. 37, no. 6, pp. 620–626, 2011.
- [2] A. Ducoin, B. Huang, and Y. L. Young, "Numerical modeling of unsteady cavitating flows around a stationary hydrofoil," *Int. J. Rotating Mach.*, vol. 2012, 2012.
- [3] E. Goncalves and R. F. Patella, "Numerical simulation of cavitating flows with homogeneous models," *Comput. Fluids*, vol. 38, no. 9, pp. 1682–1696, 2009.
- [4] Y. Iga, M. Nohmi, A. Goto, B. R. Shin, and T. Ikohagi, "Numerical Study of Sheet Cavitation Breakoff Phenomenon on a Cascade Hydrofoil," *J. Fluids Eng.*, vol. 125, no. 4, p. 643, 2003.
- [5] J. Reboud, B. Stutz, and O. Coutier, "Two-phase flow structure of cavitation: Experiment and modeling of unsteady effects," in *Third International Symposium on Cavitation*, 1998.
- [6] Z. Li, G. Zhang, W. He, and T. van Terwisga, "A numerical study of unsteady cavitation on a hydrofoil by LES and URANS method," *J. Phys. Conf. Ser.*, vol. 656, no. 1, p. 012157, Dec. 2015.
- [7] X. Long, H. Cheng, B. Ji, and R. E. A. Arndt, "Numerical investigation of attached cavitation shedding dynamics around the Clark-Y hydrofoil with the FBDCM and an

- integral method,” *Ocean Eng.*, vol. 137, pp. 247–261, Jun. 2017.
- [8] G. Wang and M. Ostoja-Starzewski, “Large eddy simulation of a sheet/cloud cavitation on a NACA0015 hydrofoil,” *Appl. Math. Model.*, vol. 31, no. 3, pp. 417–447, 2007.
- [9] Y. Saito, R. Takami, I. Nakamori, and T. Ikohagi, “Numerical analysis of unsteady behavior of cloud cavitation around a NACA0015 foil,” *Comput. Mech.*, vol. 40, no. 1, pp. 85–96, 2007.
- [10] Z. Li, M. Pourquie, and T. J. C. Van Terwisga, “A numerical study of steady and unsteady cavitation on a 2d hydrofoil,” *J. Hydrodyn. Ser. B*, vol. 22, no. 5, pp. 770–777, Oct. 2010.
- [11] V. H. Hidalgo, X. W. Luo, X. Escaler, J. Ji, and A. Aguinaga, “Numerical investigation of unsteady cavitation around a NACA 66 hydrofoil using OpenFOAM,” *IOP Conf. Ser. Earth Environ. Sci.*, vol. 22, no. 5, p. 052013, Mar. 2014.
- [12] B. Ji, X. Luo, Y. Wu, X. Peng, and Y. Duan, “Numerical analysis of unsteady cavitating turbulent flow and shedding horse-shoe vortex structure around a twisted hydrofoil,” *Int. J. Multiph. Flow*, vol. 51, pp. 33–43, May 2013.
- [13] N. Ochiai, Y. Iga, M. Nohmi, and T. Ikohagi, “Numerical Prediction of Cavitation Erosion Intensity in Cavitating Flows around a Clark Y 11.7% Hydrofoil *,” *J. Fluid Sci. Technol.*, vol. 5, no. 3, 2010.
- [14] Y. Iga, M. Nohmi, A. Goto, and T. Ikohagi, “Numerical Analysis of Cavitation Instabilities Arising in the Three-Blade Cascade,” *J. Fluids Eng.*, vol. 126, no. 3, p. 419, 2004.
- [15] Yu Fengrong, Zhang Lixiang, Zeng Yun, and Luo Zhumei, “Preliminary discussion for improving cavitating flow around hydrofoil by punching,” *Procedia Eng.*, vol. 31, pp. 261–266, 2012.
- [16] M. Hofmann, B. Stoffel, J. Friedrichs, G. Kosyna, and Others, “Similarities and Geometrical Effects on Rotating Cavitation In Two Scaled Centrifugal Pumps,” *Fourth Int. Symp. Cavitation, Pasadena, CA USA*, 2001.
- [17] H. Sun, “Numerical study of hydrofoil geometry effect on cavitating flow,” *J. Mech. Sci. Technol.*, vol. 26, no. 8, pp. 2535–2545, 2012.
- [18] M. Zangeneh, “A Compressible Three-Dimensional Design Method for Radial and Mixed Flow Turbomachinery Blades,” *Int. J. Numer. Methods Fluids*, vol. 13, no. 5, pp. 599–624, 1991.
- [19] T. Dang and V. Isgro, “Euler-Based Inverse Method for Turbomachine Blades Part 1: Two-Dimensional Cascades,” *AIAA J.*, vol. 33, no. 12, 1995.
- [20] P. J. Zwart, A. G. Gerber, and T. Belamri, “A two-phase flow model for predicting cavitation dynamics,” *Fifth Int. Conf. Multiph. Flow, Yokohama, Japan*, no. 152, 2004.
- [21] A. Kubota, H. Kato, and H. Yamaguchi, “A new modelling of cavitating flows: a numerical study of unsteady cavitation on a hydrofoil section,” *J. Fluid Mech.*, vol. 240, no. 1, p. 59, 1992.
- [22] M. Zangeneh, “A compressible three-dimensional design method for radial and mixed flow turbomachinery blades,” *Int. J. Numer. Methods Fluids*, vol. 13, no. 5, pp. 599–624, 1991.
- [23] M. Dular, B. Stoffel, and B. Širok, “Development of a cavitation erosion model,” *Wear*, vol. 261, no. 5–6, pp. 642–655, 2006.
- [24] I. J. Karassik, J. P. Messina, P. Cooper, and C. C. Heald, *Pump Handbook*. McGraw-Hill, 2001.